Available online at www.sciencedirect.com

SCIENCE DIRECT®

Journal of Sound and Vibration 281 (2005) 73–97

JOURNAL OF SOUND AND VIBRATION

www.elsevier.com/locate/jsvi

Active control of connected plates using single and multiple actuators and error sensors

John Keir[a,*], Nicole J. Kessissoglou[a], Chris J. Norwood[b]

[a]*School of Engineering, James Cook University, Townsville, QLD 4811, Australia*
[b]*Defence Science and Technology Organisation (DSTO), Aeronautical and Maritime Research Laboratory (AMRL), Melbourne, Vic. 3001, Australia*

Received 30 May 2003; received in revised form 28 November 2003; accepted 8 January 2004
Available online 8 October 2004

Abstract

Active control of the structure-borne vibration transmission in resonant, built-up structures which typically represent a ship hull is analytically and experimentally investigated. Using feedforward active control, the control performance is compared for both dependent and independent control force arrangements. Multiple actuator control forces and multiple error sensors are used to actively control the frequency response. The global response of the coupled plate structure is also presented for active control at discrete resonance frequencies.

---

1. Introduction

Many structures encountered in the engineering industry such as ship hulls, building structures and machine casing are composed of joined rectangular plates. Vibrations generated in these structures due to an external excitation are usually transmitted throughout the system. For example, the propulsion machinery (diesel engines, gas turbines, propellers) in maritime vessels generate substantial vibrations that are transmitted through the structure, which may result in

---

*Corresponding author.
E-mail address: john.keir@jcu.edu.au (J. Keir).

doi:10.1016/j.jsv.2004.01.007

structural fatigue, damage to on-board equipment, and significant noise radiation. Methods of controlling wave propagation through structures has attracted much interest in the last few decades, with the majority of the work carried out focusing on using active control techniques to attenuate the structural vibration and radiated noise associated with structures such as beams, plates and cylindrical shells [1–6]. Active control of vibratory power transmission along a semi-infinite plate using an array of control actuators and error sensors has been analytically investigated for various control arrangements [4]. It was shown that by using an array of independently driven control forces placed in a row across the plate, the harmonic vibratory power transmission in a semi-infinite plate can be reduced significantly. Active control of sound radiation from a simply supported rectangular plate has been analytically investigated [5]. The use of active control to attenuate sound radiation from a simply supported plate has also been experimentally examined [6]. In the experiments, the number of actuators used was varied so as to determine the effect on the control performance. It was shown that the position of the actuator greatly affected the structural response. Increasing the number of control actuators only slightly improved the attenuation levels at a structural resonance. Sergent and Duhamel [7] showed that the optimisation of the placement of secondary sources and error sensors can enhance the efficiency of active vibration control, and may be achieved using the cost function called the "minimax" criterion. The criterion is based on the minimisation of the largest squared pressures at a number of distributed points, and is adapted to find the most suitable placement of sources and sensors. Hiramoto et al. [8] showed that several gradient-based algorithms may also be used to formulate the optimal placement of the control sources and sensors.

This paper presents a theoretical investigation using active control to attenuate the responses associated with a coupled plate structure. The paper is an extension of previous work on the active control of a series of rectangular plates using a single control force and a single error sensor [9]. Multiple actuators and error sensors in various arrangements are used to attenuate the frequency response of a T-shaped plate. The number and location of the control forces and error sensors were investigated, and their effects on the control performance were compared. In addition, the effect of the control forces driven dependently and independently was investigated. For active control at discrete resonance frequencies, the global response of the structure was also observed. Experiments were conducted in order to validate the active control of the global response at a low resonance frequency.

2. Primary flexural displacement of a T-shaped plate

The following theory is presented for a coupled plate structure as shown in Fig. 1. The structure is made up of three finite plates joined together at right angles along a common edge at $x_i = 0$ for $i = 1$ to 3, to form a T-shaped plate. The coordinate system and forcing arrangement are also shown in Fig. 1. All three plates are simply supported along the edges $y = 0$ and $y = L_y$, and are free at the other ends corresponding to $x_i = L_{xi}$ for $i = 1$ to 3. A point force excitation of F_p was applied on plate 1 at (x_p, y_p) to analytically model the external disturbance, and is described in terms of a Dirac delta function. The plate flexural displacements w are governed by the plate classical equation

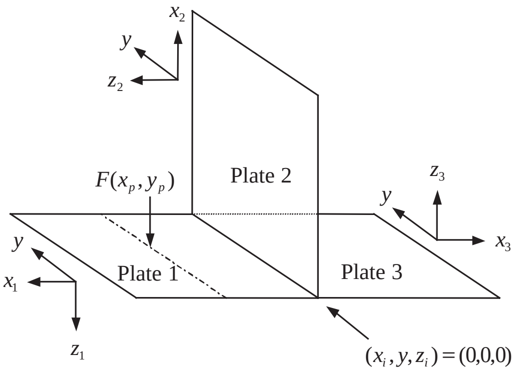

Fig. 1. T-shaped plate under point force excitation showing the sign convention for each plate.

of motion:

$$D\nabla^4 w(x,y,t) + \rho h \frac{\partial^2 w(x,y,t)}{\partial t^2} = F_p \delta(x - x_p)\delta(y - y_p)e^{j\omega t}, \tag{1}$$

where $\nabla^4 = \nabla^2\nabla^2$ and $\nabla^2 = \partial^2/\partial x^2 + \partial^2/\partial y^2$ is the Laplace operator. $D = Eh^3/12(1 - v^2)$ is the plate flexural rigidity, where E is Young's modulus, v is Poisson's ratio, ρ is the density, and h is the plate thickness. Theory has been previously presented for a generic structure corresponding to an L, T or cross-shaped plate, in order to obtain expressions for the plate flexural displacement at any location on the coupled plate structure [9]. This theory includes the boundary conditions, and the continuity and equilibrium equations at the structural junctions and driving force location.

The primary plate flexural displacement in the various sections can be described by $w_p(x,y) = F_p G_p(x,y)$. Since the plate displacement is time harmonic with radian frequency ω, the time-dependent factor $e^{j\omega t}$ is omitted in the proceeding equations. $G_p(x,y)$ is the primary transfer function and is given by [4,9]

$$G_p(x,y) = \sum_{m=1}^{\infty} \frac{2}{L_y D} \sin(k_y y_p)[\alpha_p]^{-T}_{n,10}[E^i_p] \sin(k_y y), \tag{2}$$

where m is the mode number. $k_y = m\pi/L_y$ is the wavenumber in the y-direction, and L_y is the plate width. $[\alpha_p]^{-T}_{n,10}$ corresponds to the tenth column of the inverse of the non-singular matrix $[\alpha_p]$, where $n = 1, \ldots, 16$ corresponds to the number of rows. $[\alpha_p]$ and $[E^i_p]$ are given in Appendix A.

3. Active control

For completeness of the control theory, active control arrangements are presented for both single and multiple control forces and error sensors. In addition, multiple control forces driven dependently and independently are considered.

3.1. Active control using a single control force and a single error sensor

A control point force of amplitude F_s is applied at a position (x_s, y_s) on plate 1. The general solution for the secondary plate displacement may be expressed as $w_s(x,y) = F_s G_s(x,y)$, where $G_s(x,y)$ is the secondary transfer function, and is given by [4,9]

$$G_s(x,y) = \sum_{m'=1}^{\infty} \frac{2}{L_y D} \sin(k_y y_s)[\alpha_s]^{-T}_{n,10} \left[E^i_s\right] \sin(k_y y). \tag{3}$$

G_s is now a function of mode number m'. $[\alpha_s]$ and $[E^i_s]$ are the same as $[\alpha_p]$ and $[E^i_p]$ except they are functions of mode number m', and x_p is replaced by x_s. The total flexural displacement can be obtained by adding the plate displacements induced by the primary and control forces

$$w_{\text{tot}}(x,y) = w_p(x,y) + w_s(x,y). \tag{4}$$

A cost function is developed using a feedforward adaptive least-mean-square algorithm [10]. The cost function to be minimised is the total squared plate displacement at an error sensor location (x_e, y_e), and can be expressed as a quadratic function in terms of the complex control force amplitude

$$w_{\text{tot}}(w_{\text{tot}})^* = F^*_s A_\Pi F_s + F^*_s B_\Pi F_p + F_s B^*_\Pi F^*_p + F^*_p C_\Pi F_p, \tag{5}$$

where the asterisk "*" denotes the complex conjugate, and $A_\Pi = G^*_s G_s$, $B_\Pi = G^*_s G_p$ and $C_\Pi = G^*_p G_p$. The optimal control force amplitude that results in the minimisation of the cost function can be determined by setting the partial derivatives of the cost function with respect to the real and imaginary parts of the control force to zero [10]. That is, $\partial w_{\text{tot}}(w_{\text{tot}})^*/\partial F_{s\,\text{real}} = 0$ and $\partial w_{\text{tot}}(w_{\text{tot}})^*/\partial F_{s\,\text{imag}} = 0$. The optimal control force can then be obtained as

$$F_s|_{\text{opt}} = F_{s\,\text{real}} + \mathrm{j}F_{s\,\text{imag}} = -F_p \frac{B_\Pi}{A_\Pi}. \tag{6}$$

The expression given in Eq. (6) remains the same for the various control configurations using either a single control force, or multiple dependently driven control forces. In the case of multiple dependently driven control forces, the control forces are driven in phase and with the same complex amplitude F_s. However, the quadratic terms A_Π, B_Π and C_Π change depending on the number of control forces and error sensors, and are given for several different control configurations in the proceeding sections.

3.2. Active control using a single control force and multiple error sensors

When multiple error sensors are considered, the total squared plate displacement is minimised at all error sensor locations simultaneously:

$$\begin{aligned} w_{\text{tot}}(w_{\text{tot}})^* &= \sum_{e=1}^{n} \left(w_p(x_e,y_e) + w_s(x_e,y_e)\right)\left(w_p(x_e,y_e) + w_s(x_e,y_e)\right)^* \\ &= \sum_{e=1}^{n} \left(F_p G_p(x_e,y_e) + F_s G_s(x_e,y_e)\right)\left(F_p G_p(x_e,y_e) + F_s G_s(x_e,y_e)\right)^*, \end{aligned} \tag{7}$$

where $e = 1-n$ represents the number of error sensors. The cost function terms in Eq. (5) now become

$$A_{\Pi} = \sum_{e=1}^{n} G_s^*(x_e, y_e) G_s(x_e, y_e), \tag{8}$$

$$B_{\Pi} = \sum_{e=1}^{n} G_s^*(x_e, y_e) G_p(x_e, y_e), \tag{9}$$

$$C_{\Pi} = \sum_{e=1}^{n} G_p^*(x_e, y_e) G_p(x_e, y_e). \tag{10}$$

3.3. Active control using multiple control forces driven dependently and a single error sensor

For multiple dependently driven control forces, there is still only one optimal complex control force amplitude F_s to be determined. The total plate displacement due to the primary and control forces at the error sensor location is given by

$$w_{\text{tot}} = w_p(x_e, y_e) + \sum_{j=1}^{N} w_{sj}(x_e, y_e) = F_p G_p\left(x_e, y_e\right) + F_s \sum_{j=1}^{N} G_{sj}(x_e, y_e). \tag{11}$$

G_{sj} represents the secondary transfer function for the jth control force, and is a function of mode number m_j' where $j = 1-N$ represents the number of control forces. The cost function terms in Eq. (5) now become

$$A_{\Pi} = \sum_{j=1}^{N} G_{sj}^*(x_e, y_e) \sum_{j=1}^{N} G_{sj}(x_e, y_e), \tag{12}$$

$$B_{\Pi} = \sum_{j=1}^{N} G_{sj}^*(x_e, y_e) G_p(x_e, y_e), \tag{13}$$

$$C_{\Pi} = G_p^*(x_e, y_e) G_p(x_e, y_e). \tag{14}$$

3.4. Active control of multiple control forces driven dependently and multiple error sensors

When multiple dependently driven control forces and multiple error sensors are used for the active control, the cost function to be minimised is the total squared plate displacement due to all forces at all the error sensor locations simultaneously

$$\begin{aligned} w_{\text{tot}}(w_{\text{tot}})^* &= \sum_{e=1}^{n} \left(w_p(x_e, y_e) + \sum_{j=1}^{N} w_{sj}(x_e, y_e) \right) \left(w_p(x_e, y_e) + \sum_{j=1}^{N} w_{sj}(x_e, y_e) \right)^* \\ &= \sum_{e=1}^{n} \left(F_p G_p(x_e, y_e) + F_s \sum_{j=1}^{N} G_{sj}(x_e, y_e) \right) \left(F_p G_p(x_e, y_e) + F_s \sum_{j=1}^{N} G_{sj}(x_e, y_e) \right)^*, \end{aligned} \tag{15}$$

where n is the number of error sensors and N is the number of control forces. The quadratic function terms in the cost function become

$$A_\Pi = \sum_{e=1}^{n}\left(\sum_{j=1}^{N} G_{sj}^*(x_e, y_e)\sum_{j=1}^{N} G_{sj}(x_e, y_e)\right), \tag{16}$$

$$B_\Pi = \sum_{e=1}^{n}\left(\sum_{j=1}^{N} G_{sj}^*(x_e, y_e)G_p(x_e, y_e)\right), \tag{17}$$

$$C_\Pi = \sum_{e=1}^{n} G_p^*(x_e, y_e)G_p(x_e, y_e). \tag{18}$$

3.5. Active control using multiple control forces driven independently and a single error sensor

Using a control configuration consisting of independently driven control forces, the total displacement at the error sensor location (x_e, y_e) is given by the sum of the displacements due to the primary force and the secondary forces

$$w_{\mathrm{tot}} = w_p(x_e, y_e) + \sum_{j=1}^{N} w_{sj}(x_e, y_e) = F_p G_p(x_e, y_e) + \sum_{j=1}^{N} F_{sj} G_{sj}(x_e, y_e), \tag{19}$$

where F_{sj} are the complex control force amplitudes to be optimised. In the case of two independently driven control forces, there are two control force amplitudes, corresponding to F_{s1} and F_{s2} to be optimised. To find the optimal control force amplitudes, the partial derivatives of the total squared plate displacement with respect to the real and imaginary parts of the control forces are set to zero as described in Section 3.1, resulting in

$$\frac{\partial w_{\mathrm{tot}}(w_{\mathrm{tot}})^*}{\partial F_{s1\,\mathrm{real}}} = 2G_{s1}^* G_{s1} F_{s1\,\mathrm{real}} + G_{s1} G_{s2}^* F_{s2}^* + G_{s1}^* G_{s2} F_{s2} + F_p G_p G_{s1}^* + F_p^* G_p^* G_{s1} = 0, \tag{20}$$

$$\frac{\partial w_{\mathrm{tot}}(w_{\mathrm{tot}})^*}{\partial F_{s1\,\mathrm{imag}}} = 2G_{s1}^* G_{s1} F_{s1\,\mathrm{imag}} + \mathrm{j}G_{s1} G_{s2}^* F_{s2}^* - \mathrm{j}G_{s1}^* G_{s2} F_{s2} - \mathrm{j}F_p G_p G_{s1}^* + \mathrm{j}F_p^* G_p^* G_{s1} = 0, \tag{21}$$

$$\frac{\partial w_{\mathrm{tot}}(w_{\mathrm{tot}})^*}{\partial F_{s2\,\mathrm{real}}} = 2G_{s2}^* G_{s2} F_{s2\,\mathrm{real}} + G_{s2} G_{s1}^* F_{s1}^* + G_{s2}^* G_{s1} F_{s1} + F_p G_p G_{s2}^* + F_p^* G_p^* G_{s2} = 0, \tag{22}$$

$$\frac{\partial w_{\mathrm{tot}}(w_v)^*}{\partial F_{s2\,\mathrm{imag}}} = 2G_{s2}^* G_{s2} F_{s2\,\mathrm{imag}} + \mathrm{j}G_{s2} G_{s1}^* F_{s1}^* - \mathrm{j}G_{s2}^* G_{s1} F_{s1} - \mathrm{j}F_p G_p G_{s2}^* + \mathrm{j}F_p^* G_p^* G_{s2} = 0. \tag{23}$$

Combining the real and imaginary components of the control forces in Eqs. (20)–(23) results in

$$G_{s1}^* G_{s1} F_{s1} + G_{s1}^* G_{s2} F_{s2} = -F_p G_{s1}^* G_p, \tag{24}$$

$$G_{s2}^* G_{s1} F_{s1} + G_{s2}^* G_{s2} F_{s2} = -F_p G_{s2}^* G_p. \tag{25}$$

Eqs. (24) and (25) may be rearranged into matrix form such that the set of optimal independently driven control forces may be obtained

$$\begin{bmatrix} F_{s1} \\ F_{s2} \end{bmatrix} = -F_p \begin{bmatrix} G_{s1}^* G_{s1} & G_{s1}^* G_{s2} \\ G_{s2}^* G_{s1} & G_{s2}^* G_{s2} \end{bmatrix}^{-1} \begin{bmatrix} G_{s1}^* G_p \\ G_{s2}^* G_p \end{bmatrix}. \tag{26}$$

For N number of independently driven control forces, the optimal control force amplitudes can be obtained by

$$\begin{bmatrix} F_{s1} \\ \vdots \\ \vdots \\ F_{sN} \end{bmatrix} = -F_p \begin{bmatrix} G_{s1}^* G_{s1} & \dots & \dots & G_{s1}^* G_{sN} \\ \vdots & \ddots & & \vdots \\ \vdots & & \ddots & \vdots \\ G_{sN}^* G_{s1} & \cdots & \cdots & G_{sN}^* G_{sN} \end{bmatrix}^{-1} \begin{bmatrix} G_{s1}^* G_p \\ \vdots \\ \vdots \\ G_{sN}^* G_p \end{bmatrix}. \tag{27}$$

3.6. *Active control using multiple control forces driven independently and multiple error sensors*

When multiple error sensors and multiple independently driven control forces are used, the total plate displacement at the error sensor locations becomes

$$w_{\text{tot}} = \sum_{e=1}^{n} \left(w_p(x_e, y_e) + \sum_{j=1}^{N} w_s(x_e, y_e) \right) = \sum_{e=1}^{n} \left(F_p G_p(x_e, y_e) + \sum_{j=1}^{N} F_{sj} G_{sj}(x_e, y_e) \right), \tag{28}$$

where n is the number of error sensors and N is the number of independently driven control forces. The optimal control force amplitudes can be obtained by

$$\begin{bmatrix} F_{s1} \\ \vdots \\ \vdots \\ F_{sN} \end{bmatrix} = -F_p \begin{bmatrix} \sum_{e=1}^{n} (G_{s1}^* G_{s1}) & \dots & \dots & \sum_{e=1}^{n} (G_{s1}^* G_{sN}) \\ \vdots & \ddots & & \vdots \\ \vdots & & \ddots & \vdots \\ \sum_{e=1}^{n} (G_{sN}^* G_{s1}) & \cdots & \cdots & \sum_{e=1}^{n} (G_{sN}^* G_{sN}) \end{bmatrix}^{-1} \begin{bmatrix} \sum_{e=1}^{n} (G_{s1}^* G_p) \\ \vdots \\ \vdots \\ \sum_{e=1}^{n} (G_{sN}^* G_p) \end{bmatrix}. \tag{29}$$

4. Experimental arrangement

An experimental test rig consisting of three aluminium plates connected in a T-shaped was constructed. The T-shaped plate was formed by welding together three 600 mm × 500 mm plates along a common 500 mm edge. Each plate has a thickness of 2 mm. The boundary conditions were designed to simulate simply supported on parallel sides of the T-shaped plate. The simply supported boundary conditions were achieved by screwing the edges of the plate to z-sections at regular intervals of 25 mm. The z-sections needed to be flexible and were constructed of 0.8 mm

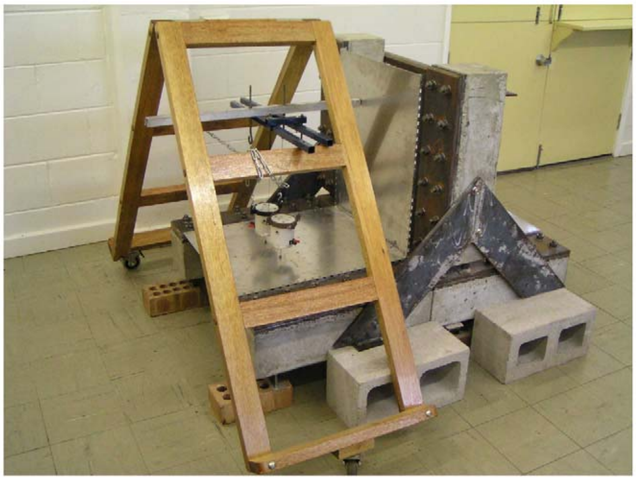

Fig. 2. Photograph of the T-shaped plate experimental rig, showing the primary and control shakers and the structural boundaries conditions.

thick aluminium. The lower flange edges of the z-sections were clamped between concrete blocks. This construction has been previously shown to give a good approximation of simply supported boundary conditions, as the z-sections are stiff for in-plane vibration, but are sufficiently flexible for rotation [11]. The input disturbance shaker and the control shakers were positioned vertically over plate 1 of the T-shaped plate so that only flexural vibration in the plates was generated. Fig. 2 is a photograph of T-shaped experimental rig, showing the primary and control shakers and the structural boundaries.

A Causal Systems EZ-ANC was used as the active controller in the experiments [12]. The EZ-ANC controller is an adaptive feedforward active control system that is based on a filtered-X version of the adaptive least-mean-square (LMS) algorithm. Brüel & Kjær Type 4375 accelerometers of 2 g weight were used as the error sensors. The accelerometers were attached to the plate using beeswax, with minimal mass loading due to their 2 g weight. The signals from the accelerometers were conditioned by a Nexus Type 2692A charge conditioning amplifier, and the results were displayed in a Brüel & Kjær Type 2032 dual channel signal analyser.

5. Results and discussion

The material parameters of aluminium used in the modelling are density $\rho = 2700\,\mathrm{kg/m^3}$, Young's modulus $E = 7.1 \times 10^{10}\,\mathrm{N/m^2}$ and Poisson's ratio $v = 0.3$. Hysteretic damping in the structure was included by using a complex Young's modulus $E(1 + \mathrm{j}\eta)$, where $\eta = 0.001$ is the structural loss factor. The same dimensions were used as for the experiments, corresponding to $L_x = 600$ mm, $L_y = 500$ mm and $h = 2$ mm. In each control case, the primary shaker was placed on plate 1 at a fixed location (in metres) of $(x_p, y_p) = (0.371, 0.19)$, which resulted in simultaneous excitation of all the structural modes. Results are presented in terms of acceleration levels (in dB). The acceleration is converted to dB using $L_a = 20 \log 10(a/a_{\mathrm{ref}})$, where $a_{\mathrm{ref}} = 10^{-6}$ m/s^2 is the internationally accepted reference value [13]. The primary acceleration distributions in each control case are measured at a location $(x_p, y_p) = (0.23, 0.19)$, which results in simultaneous measurement of all the structural modes.

Fig. 3 displays the primary and controlled acceleration distributions for a frequency range up to 400 Hz for the T-shaped plate when a single error sensor was placed on plate 2 at $(x_{e1}, y_{e1}) = (0.23, 0.25)$ (dotted line), or at $(x_{e1}, y_{e1}) = (0.36, 0.4)$ (dashed line). The control force was positioned in line with the primary force in the x-direction on plate 1, and in a symmetrical arrangement along the plate width, at $(x_{s1}, y_{s1}) = (0.371, 0.31)$. When the error sensor is placed on plate 2 at the first control set-up corresponding to $(x_{e1}, y_{e1}) = (0.23, 0.25)$, it can be shown that the control performance becomes independent of frequency. This control performance is attributed to the symmetry of the primary and control force locations with respect to the simply supported boundary conditions, and the location of the error sensor at the midway point along the width of the plate [9]. The control performance deteriorates when the error sensor is shifted from the midway point of $y_e = L_y/2 = 0.25$ m. Under the symmetrical control arrangement, the control force amplitude is always unity. These control results are also confirmed when the error sensor was placed at a midway point of $y_e = 0.25$ m on plates 1 and 3. When the control arrangement is

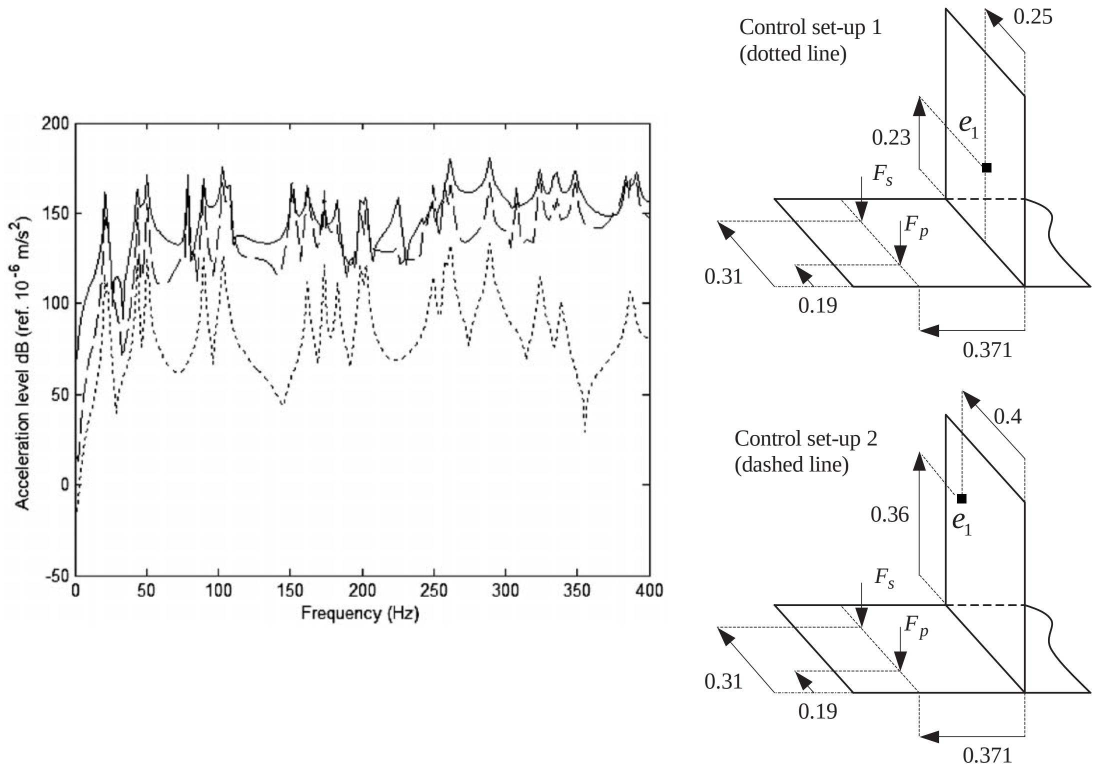

Fig. 3. Primary (solid line) and controlled frequency responses for the T-shaped plate using primary and control forces located at $(x_p, y_p) = (0.371, 0.19)$ and $(x_{s1}, y_{s1}) = (0.371, 0.31)$ respectively, for an error sensor located on plate 2 at $(x_{e1}, y_{e1}) = (0.23, 0.25)$ (dotted line), or $(x_{e1}, y_{e1}) = (0.36, 0.4)$ (dashed line).

not symmetrical with respect to the primary force location, the control force amplitude fluctuates with frequency.

Fig. 4 compares the primary and controlled acceleration distributions for a frequency range up to 400 Hz for the T-shaped plate when a single error sensor was placed on plate 2 at $(x_{e1}, y_{e1}) = (0.23, 0.19)$ (dashed line), and two error sensors were placed on plate 2 at $(x_{e1}, y_{e1}) = (0.23, 0.19)$ and $(x_{e2}, y_{e2}) = (0.23, 0.31)$ (dotted line). It can be seen that that the control performance deteriorates when one control force and multiple error sensors are used. This is due to the fact that the single control force has to divide its efforts between the two error signals such that the total squared plate displacement at each error sensor location is minimised.

The effect of the error sensor locations was initially investigated using two dependently driven control forces to simultaneously minimise the response at two error sensors. Fig. 5 presents the primary and controlled acceleration distributions for a frequency range up to 400 Hz for the T-shaped plate. The two control forces are fixed on plate 1 at the same x-location as the primary force at $(x_{s1}, y_{s1}) = (0.371, 0.25)$ and $(x_{s2}, y_{s2}) = (0.371, 0.31)$. Two error sensors positioned on plate 2 at $(x_{e1}, y_{e1}) = (0.23, 0.19)$, $(x_{e2}, y_{e2}) = (0.23, 0.31)$ (dotted line), are compared with the sensors located at $(x_{e1}, y_{e1}) = (0.23, 0.25)$, $(x_{e2}, y_{e2}) = (0.28, 0.25)$ (dashed line). The results show

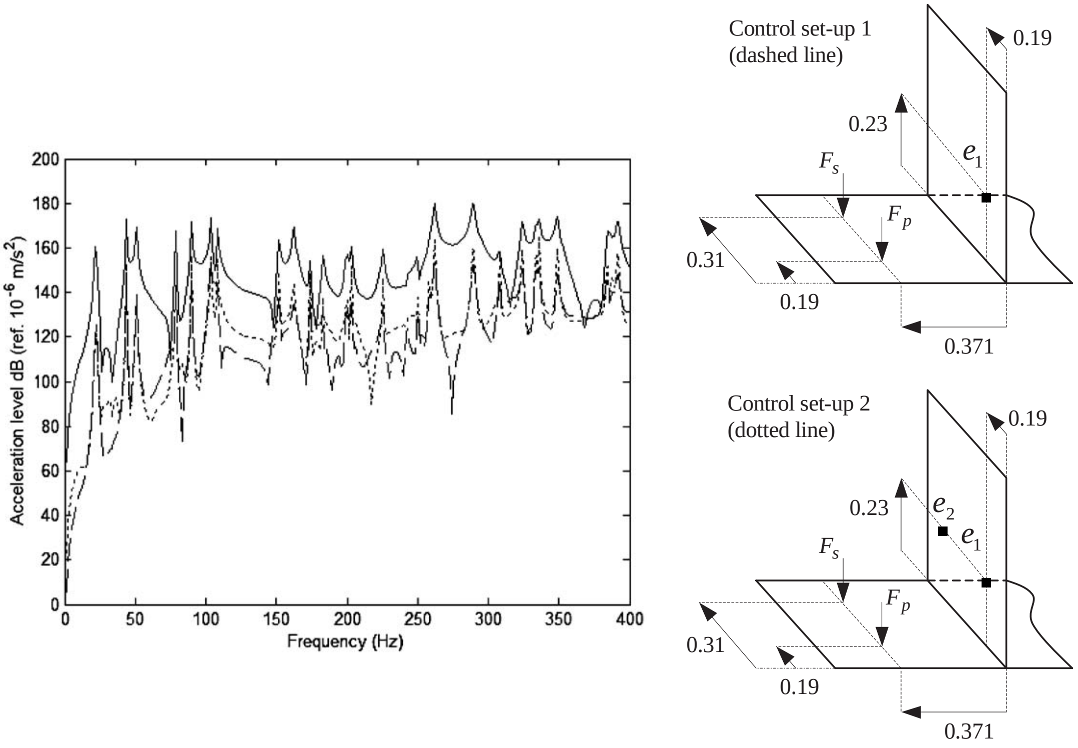

Fig. 4. Primary (solid line) and controlled frequency response for the T-shaped plate using primary and control forces located at $(x_p, y_p) = (0.371, 0.19)$ and $(x_{s1}, y_{s1}) = (0.371, 0.31)$ respectively, and for an error sensor located on plate 2 at $(x_{e1}, y_{e1}) = (0.23, 0.19)$ (dashed line) and two error sensors located on plate 2 at $(x_{e1}, y_{e1}) = (0.23, 0.19)$ and $(x_{e2}, y_{e2}) = (0.23, 0.31)$ (dotted line).

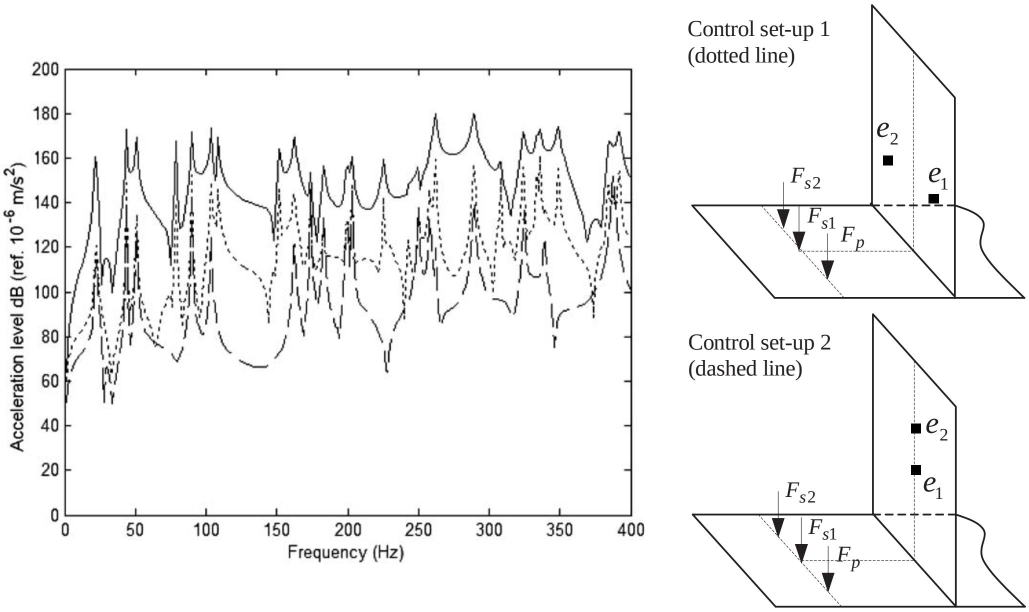

Fig. 5. Primary (solid line) and controlled frequency responses for the T-shaped plate using two dependently driven control forces and two error sensors located on plate 2 at $(x_{e1}, y_{e1}) = (0.23, 0.19)$, $(x_{e2}, y_{e2}) = (0.23, 0.31)$ (dotted line), and $(x_{e1}, y_{e1}) = (0.23, 0.25)$, $(x_{e2}, y_{e2}) = (0.28, 0.25)$ (dashed line).

that aligning the error sensors at the midway point along the width of the plate corresponding to $y_e = L_y/2 = 0.25$ m produces better attenuation levels than when the error sensors are moved away from the midway point. The corresponding optimum control force amplitudes are presented in Fig. 6 for the two combinations. Large control force amplitudes are required at various discrete resonance frequencies when the error sensors were not positioned midway along the width of the plate. When the error sensors are located at the midway point, the control force amplitude for two dependently driven control forces is fairly constant at 0.5. This means that each control force is being driven at around half the amplitude of the primary force, and is also being driven at around half the amplitude of the optimal control force using the symmetrical control arrangement consisting of a single control force and a single error sensor, as presented in the first control set-up in Fig. 3.

The effect of the control force locations was then investigated for two fixed error sensors located on plate 2 at $(x_{e1}, y_{e1}) = (0.23, 0.19)$, $(x_{e2}, y_{e2}) = (0.23, 0.31)$. Two dependently driven control forces located in line with the primary force at $(x_{s1}, y_{s1}) = (0.371, 0.25)$, $(x_{s2}, y_{s2}) = (0.371, 0.31)$ (dashed line) were compared with two arbitrarily located forces at $(x_{s1}, y_{s1}) = (0.17, 0.4)$, $(x_{s2}, y_{s2}) = (0.45, 0.29)$ (dotted line). Fig. 7 shows that changing the control force locations has very little effect on the control performance. This result was also observed using two independently driven control forces. Hence, the use of two control forces to minimise the response at two error sensor locations will result in global attenuation of the primary frequency response.

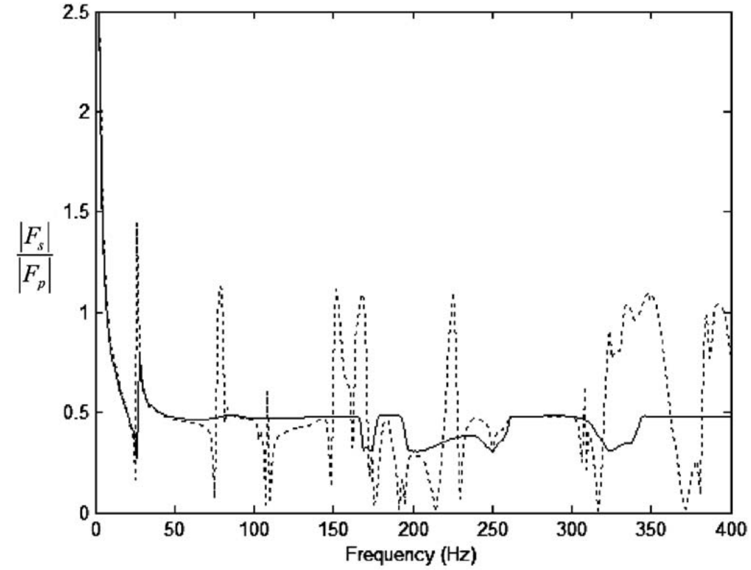

Fig. 6. Optimal control force amplitude using two dependently driven control forces and two error sensors located on plate 2 at $(x_{e1}, y_{e1}) = (0.23, 0.19)$, $(x_{e2}, y_{e2}) = (0.23, 0.31)$ (dotted line), and $(x_{e1}, y_{e1}) = (0.23, 0.25)$, $(x_{e2}, y_{e2}) = (0.28, 0.25)$ (solid line).

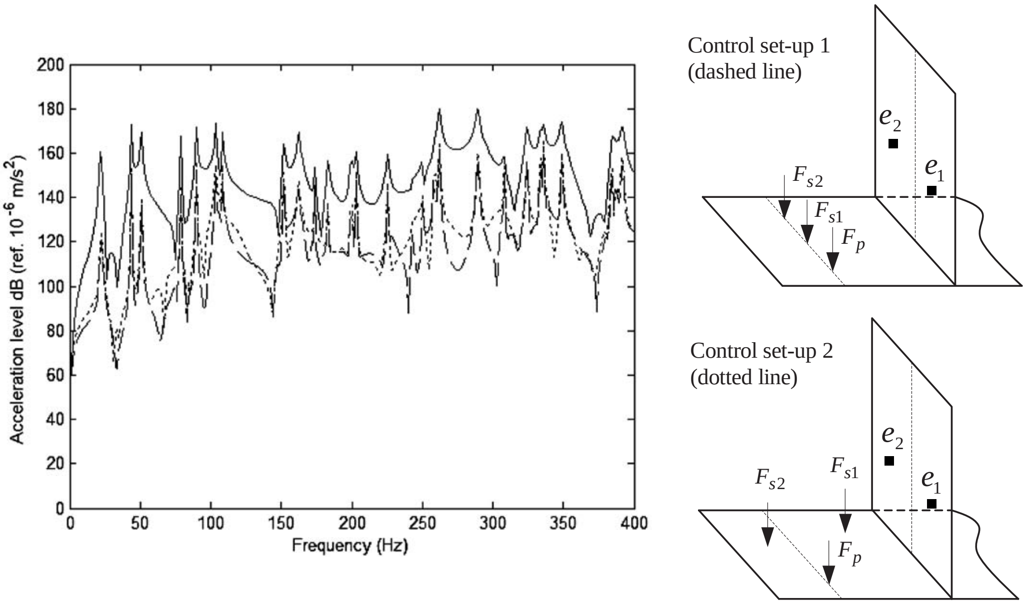

Fig. 7. Primary (solid line) and controlled frequency responses for the T-shaped plate using two dependently driven control forces located on plate 1 at $(x_{s1}, y_{s1}) = (0.371, 0.25)$, $(x_{s2}, y_{s2}) = (0.371, 0.31)$ (dashed line), and $(x_{s1}, y_{s1}) = (0.17, 0.4)$, $(x_{s2}, y_{s2}) = (0.45, 0.29)$ (dotted line).

The effect of varying the number of dependently driven control forces was then investigated for fixed error sensor positions. Further investigation shows that the use of three control forces and two error sensors produced no significant improvement in the control performance when compared to the two control force, two error sensor arrangement. Slightly higher attenuation levels can be achieved using a control set-up consisting of three control forces and three error sensors compared to using two control forces and two error sensors.

Figs. 8 and 9 compare the performance for two control forces driven dependently and independently. In Fig. 8, the control application is relatively symmetrical with respect to the primary force location, with the control forces located in-line with the primary force on plate 1 at $(x_{s1}, y_{s1}) = (0.371, 0.25)$ and $(x_{s2}, y_{s2}) = (0.371, 0.31)$, and the error sensors are located on plate 2 at $(x_{e1}, y_{e1}) = (0.23, 0.25)$, $(x_{e2}, y_{e2}) = (0.28, 0.25)$. In Fig. 9, the control forces and error sensors are arbitrarily located, with the control forces located in line with the primary force on plate 1 at $(x_{s1}, y_{s1}) = (0.17, 0.4)$ and $(x_{s2}, y_{s2}) = (0.45, 0.29)$, and the error sensors located on plates 2 and 3 respectively at $(x_{e1}, y_{e1}) = (0.17, 0.19)$ and $(x_{e2}, y_{e2}) = (0.36, 0.4)$. With the relatively symmetrical control arrangement (Fig. 8), the attenuation levels achieved are very similar using dependent control forces (dotted line) or independently driven control forces (dashed line). However, for any arbitrary control arrangement as shown in Fig. 9, the independently driven control force arrangement (dashed line) produces significantly better attenuation levels than the dependently driven control set-up (dotted line).

To investigate the effect of active control on the global response of the T-shaped plate, a low resonance frequency of 90 Hz was examined. This is the fourth natural frequency of the T-shaped plate, and corresponds to mode (3,1) of each plate. Various combinations of control force and error sensor arrangements were used, and their effect on control performance was observed. Fig. 10 shows that the uncontrolled response for the resonance frequency of 90 Hz has no nodal

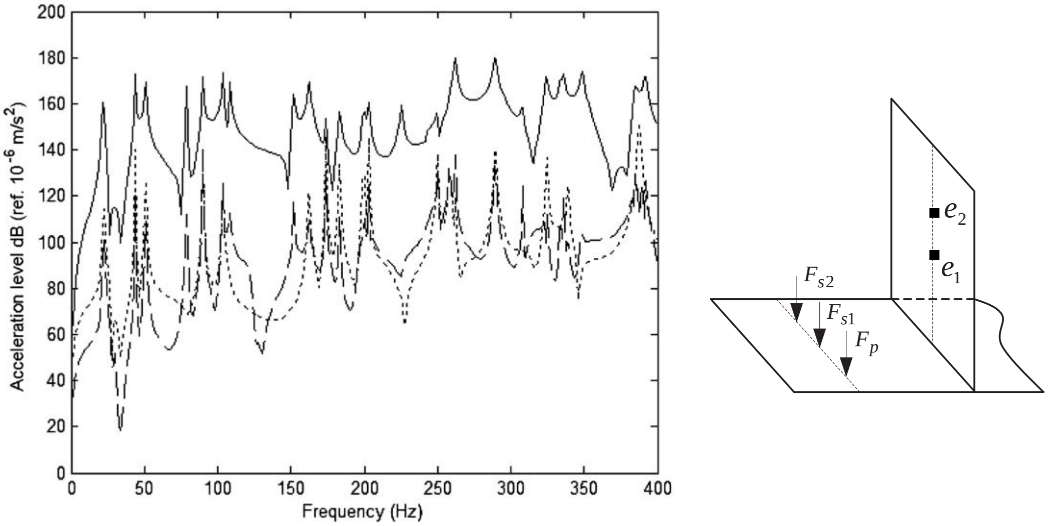

Fig. 8. Primary (solid line) and controlled frequency responses for the T-shaped plate using two dependently (dotted line) and two independently (dashed line) driven control forces located at $(x_{s1}, y_{s1}) = (0.371, 0.25)$ and $(x_{s2}, y_{s2}) = (0.371, 0.31)$ and two error sensors located on plate 2 at $(x_{e1}, y_{e1}) = (0.23, 0.25)$, $(x_{e2}, y_{e2}) = (0.28, 0.25)$.

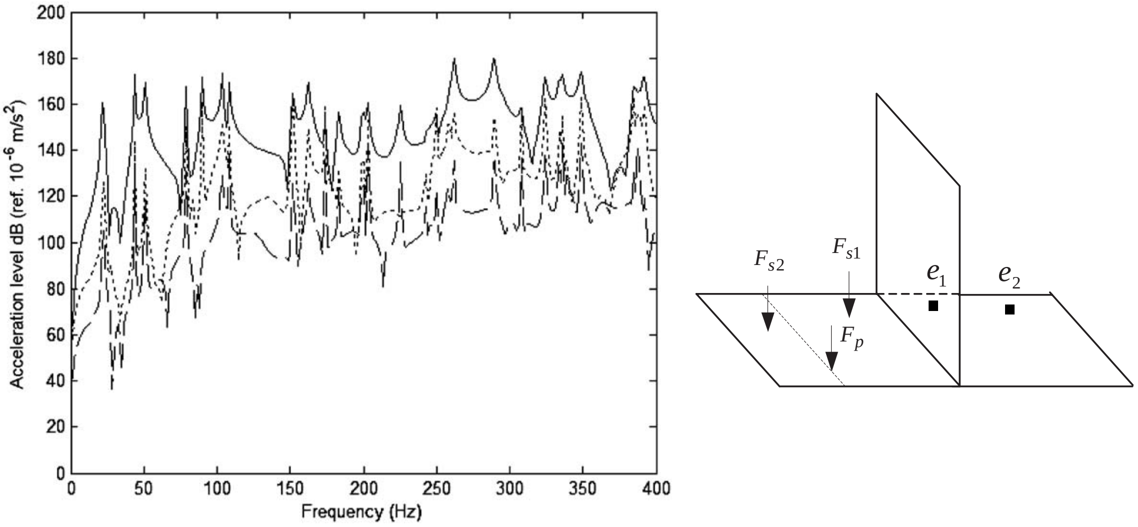

Fig. 9. Primary (solid line) and controlled frequency responses for the T-shaped plate using two dependently (dotted line) and two independently (dashed line) driven control forces located at $(x_{s1}, y_{s1}) = (0.17, 0.4)$ and $(x_{s2}, y_{s2}) = (0.45, 0.29)$, and two error sensors located on plates 2 and 3, respectively at $(x_{e1}, y_{e1}) = (0.17, 0.19)$ and $(x_{e2}, y_{e2}) = (0.36, 0.4)$.

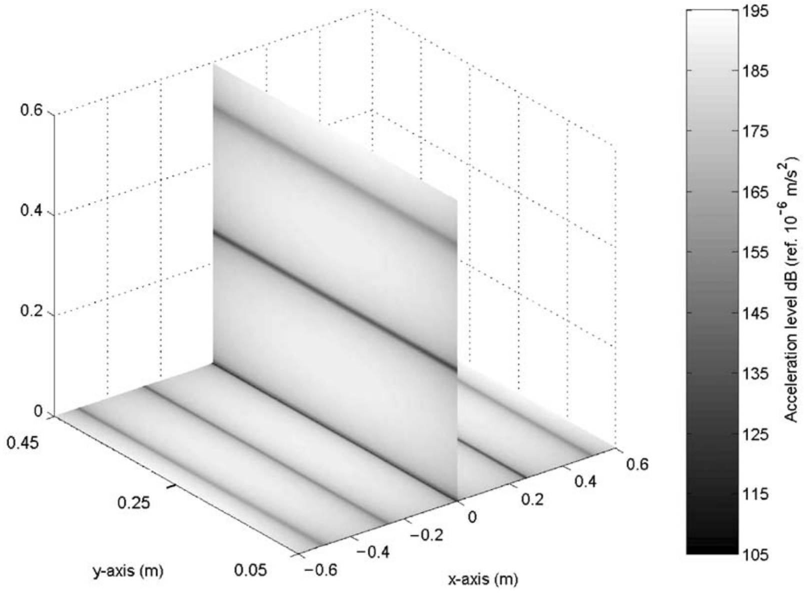

Fig. 10. Contour plot of the uncontrolled response at 90 Hz (analytical).

lines running along the x-direction. Figs. 11 and 12 show the controlled responses for the resonance frequency of 90 Hz for two different control configurations, each consisting of one error sensor and one control force. In both cases, the control force was placed in-line along the

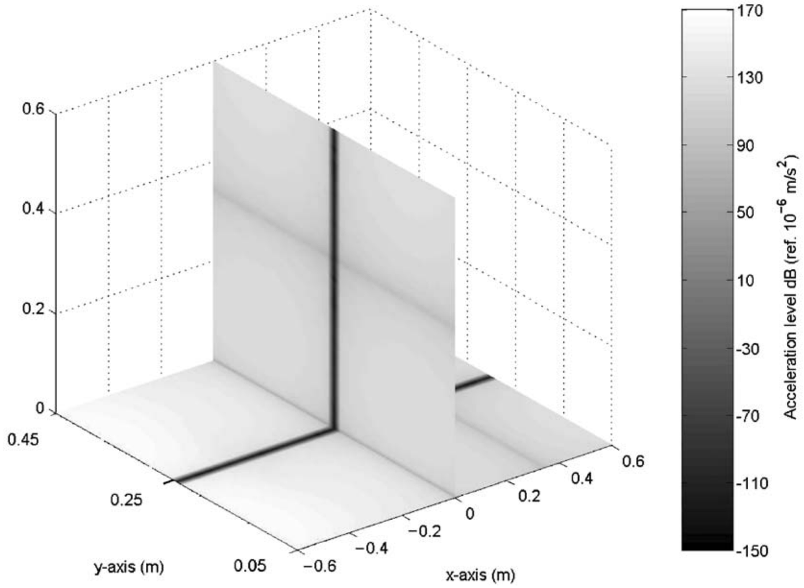

Fig. 11. Contour plot of the controlled response at 90 Hz for one control force at $(x_{s1}, y_{s1}) = (0.371, 0.31)$ and an error sensor location of $(x_{e1}, y_{e1}) = (0.23, 0.25)$.

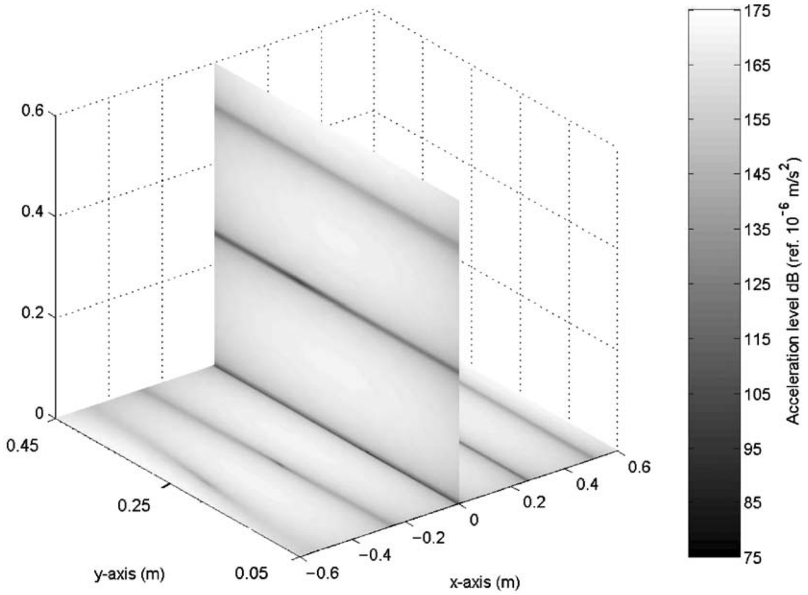

Fig. 12. Contour plot of the controlled response at 90 Hz for one control force at $(x_{s1}, y_{s1}) = (0.371, 0.31)$ and an error sensor location of $(x_{e1}, y_{e1}) = (0.43, 0.375)$.

x-direction with the primary force at $(x_s, y_s) = (0.371, 0.31)$, and is also in a symmetrical arrangement with respect to the simply supported boundary conditions. Fig. 11 shows that global attenuation was achieved when the error sensor was placed on plate 2 at $(x_{e1}, y_{e1}) = (0.23, 0.25)$, which corresponds to the midway point along the width of the T-shaped plate. This symmetrical control arrangement with respect to the simply supported boundary conditions produces the best control results for the one control force, one error sensor application [9]. Fig. 12 displays the controlled response when the error sensor was randomly placed on plate 2 at $(x_{e2}, y_{e2}) = (0.43, 0.375)$. Global attenuation is still achieved, however the control performance deteriorates once the error sensor is moved away from the symmetrical arrangement of $y_e = 0.25$ corresponding to the midway point along the plate width.

Figs. 13 and 14 show the contour plots of the attenuation levels using two dependently driven control forces located at $(x_{s1}, y_{s1}) = (0.371, 0.25)$ and $(x_{s2}, y_{s2}) = (0.371, 0.31)$, and two error sensors positioned on plate 2 at $(x_{e1}, y_{e1}) = (0.23, 0.19)$ and $(x_{e2}, y_{e2}) = (0.23, 0.31)$ (Fig. 13), and $(x_{e1}, y_{e1}) = (0.23, 0.25)$ and $(x_{e2}, y_{e2}) = (0.28, 0.25)$ (Fig. 14). In each case, global attenuation was achieved, and the control performance is not as dependent on the error sensor locations compared with using a single control force and a single error sensor. The improvement in control performance by using three control forces and multiple error sensors as opposed to two control forces and two error sensors is negligible. Fig. 15 displays the contour plot of the controlled response for the same control arrangement as Fig. 14, but with the control forces driven independently. Global attenuation was also achieved. The independently driven control forces achieved slightly better overall attenuation levels than the dependently driven control forces.

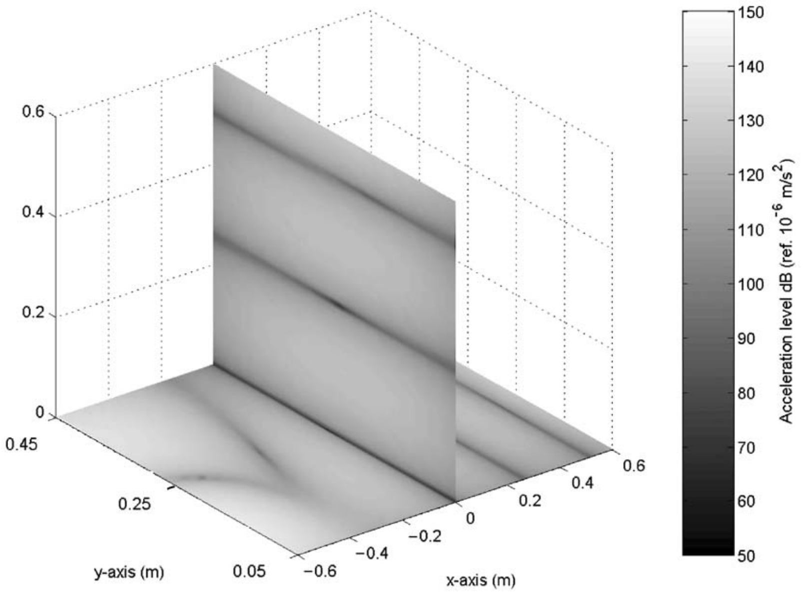

Fig. 13. Contour plot of the controlled response at 90 Hz for two dependently driven control forces at $(x_{s1}, y_{s1}) = (0.371, 0.31)$, $(x_{s2}, y_{s2}) = (0.371, 0.25)$ and two error sensors located at $(x_{e1}, y_{e1}) = (0.23, 0.19)$ and $(x_{e2}, y_{e2}) = (0.23, 0.31)$.

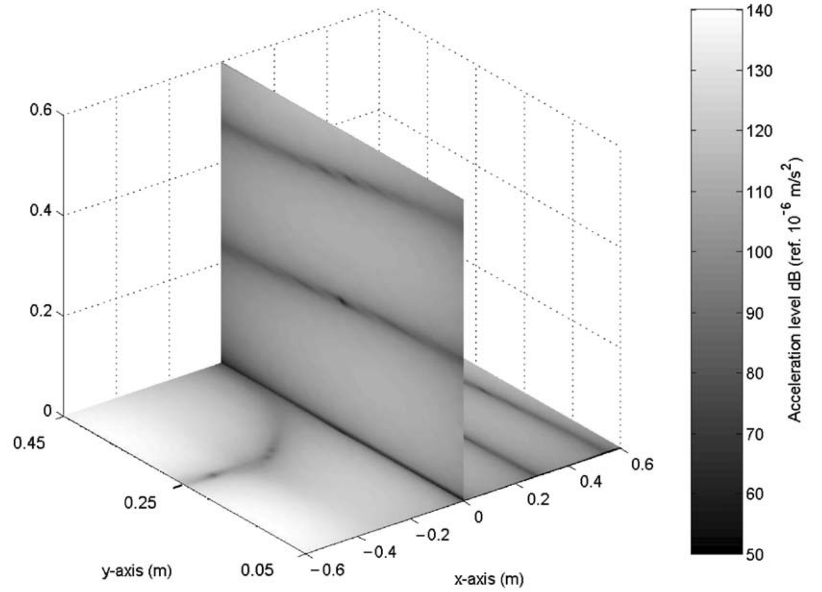

Fig. 14. Contour plot of the controlled response at 90 Hz for two dependently driven control forces at $(x_{s1}, y_{s1}) = (0.371, 0.31)$, $(x_{s2}, y_{s2}) = (0.371, 0.25)$ and two error sensors located at $(x_{e1}, y_{e1}) = (0.23, 0.25)$ and $(x_{e2}, y_{e2}) = (0.28, 0.25)$.

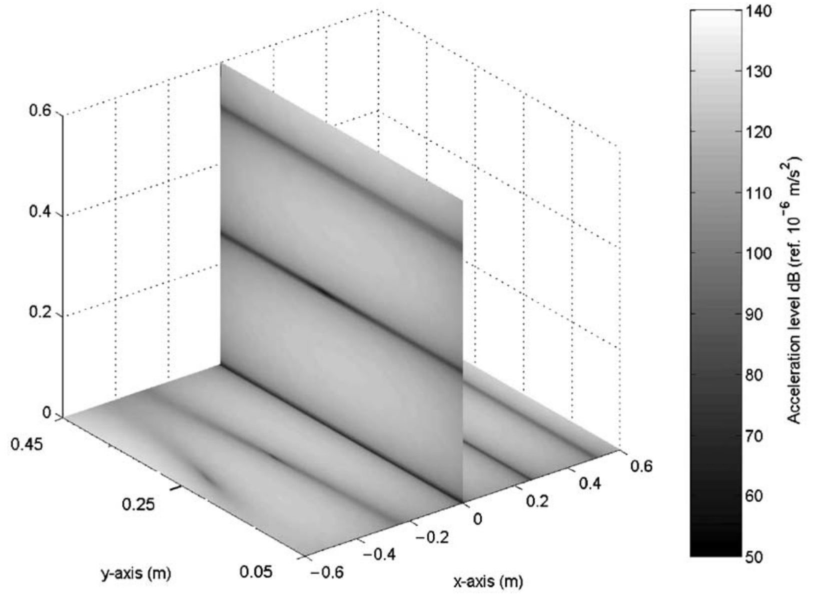

Fig. 15. Contour plot of the controlled response at 90 Hz for two independently driven control forces at $(x_{s1}, y_{s1}) = (0.371, 0.31)$, $(x_{s2}, y_{s2}) = (0.371, 0.25)$ and two error sensors located at $(x_{e1}, y_{e1}) = (0.23, 0.25)$ and $(x_{e2}, y_{e2}) = (0.28, 0.25)$.

When the control forces and error sensors are arbitrarily located, the attenuation levels using two independently driven control forces are significantly greater than those achieved using dependently driven control forces.

Active control experiments were conducted to confirm the analytical results. The contour plot at a low resonance frequency of 53.13 Hz was experimentally obtained (Fig. 16). This is the second natural frequency of the T-shaped plate, and corresponds to mode (2,1) of each plate. The same control arrangements were used in the experiments as for the control force and error sensor combinations used in the analytical investigation. Figs. 17 and 18 show the controlled responses obtained experimentally at the resonance frequency of 53.13 Hz, for a fixed control force location, and an optimally and arbitrarily located error sensor. Fig. 17 shows that significantly greater attenuation levels are achieved (around 15 dB globally over the entire plate's surface) under the symmetrical control arrangement with respect to the simply supported boundary conditions. This symmetrical control arrangement corresponds to the primary and control forces positioned at the same x-location in plate 1 and in a symmetrical arrangement in the y-direction (between the simply supported parallel edges). The error sensor is located in the far -field of the forces, but midway between the forces which corresponds to the midway point along the width of the plate ($y_e = L_y/2$). It is important to note that this symmetrical control arrangement works well when there is no nodal line running along the x-direction at the midway point along the width of the plate, that is, at $y_e = L_y/2$. The arbitrary error sensor location of (0.43, 0.375) is close to the nodal line on plate 2, and the contour plot of the controlled response shows an increase in the overall vibration levels of the plate (Fig. 18).

Figs. 19 and 20 show the contour plot of the controlled response obtained experimentally at 53.13 Hz, for two dependently driven control forces at $(x_{s1}, y_{s1}) = (0.371, 0.25)$,

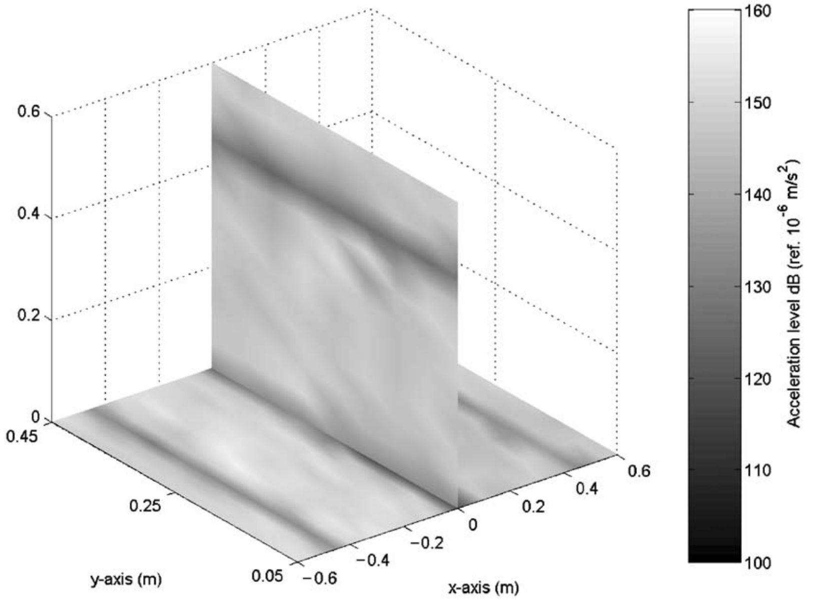

Fig. 16. Experimental contour plot of the uncontrolled response at 53.13 Hz.

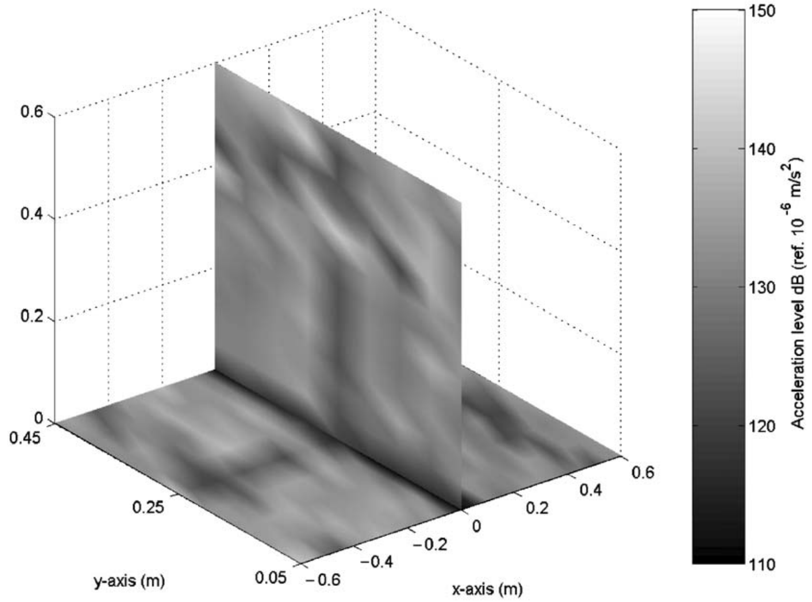

Fig. 17. Experimental contour plot of the controlled response at 53.13 Hz for one control force at $(x_{s1}, y_{s1}) = (0.371, 0.31)$ and an error sensor location of $(x_{e1}, y_{e1}) = (0.23, 0.25)$.

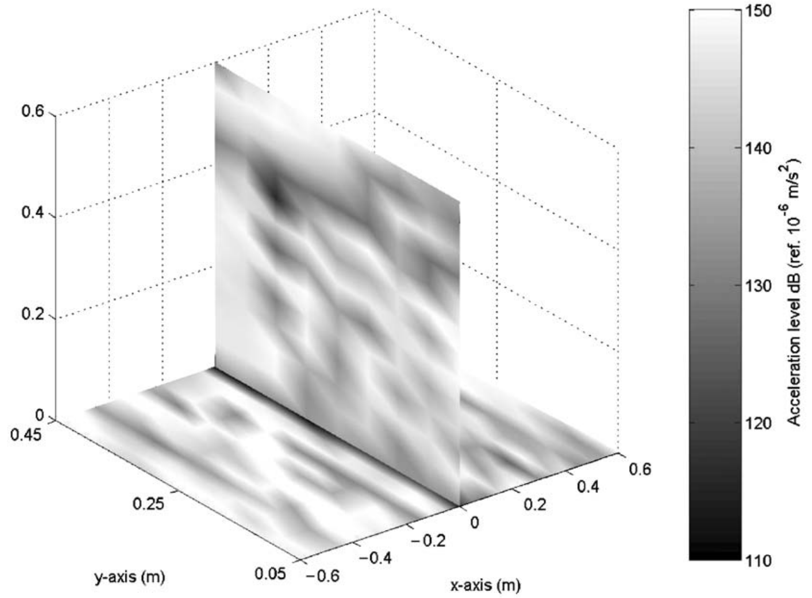

Fig. 18. Contour plot of the controlled response at 53.13 Hz for one control force at $(x_{s1}, y_{s1}) = (0.371, 0.31)$ and an error sensor location of $(x_{e1}, y_{e1}) = (0.43, 0.375)$.

$(x_{s2}, y_{s2}) = (0.371, 0.31)$, and two error sensors positioned on plate 2 at $(x_{e1}, y_{e1}) = (0.23, 0.19)$, $(x_{e2}, y_{e2}) = (0.23, 0.31)$ (Fig. 19) and $(x_{e1}, y_{e1}) = (0.23, 0.25)$, $(x_{e2}, y_{e2}) = (0.28, 0.25)$ (Fig. 20). Global attenuation of the T-shaped plate is achieved in both cases, although better attenuation is

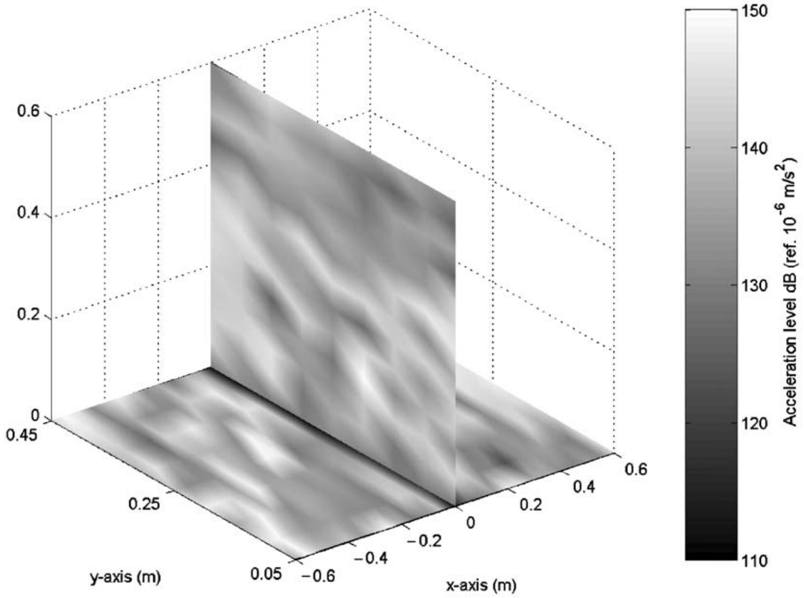

Fig. 19. Contour plot of the controlled response at 53.13 Hz for two dependently driven control forces at $(x_{s1}, y_{s1}) = (0.371, 0.25)$, $(x_{s2}, y_{s2}) = (0.371, 0.31)$ and two error sensors located at $(x_{e1}, y_{e1}) = (0.23, 0.19)$ and $(x_{e2}, y_{e2}) = (0.23, 0.31)$.

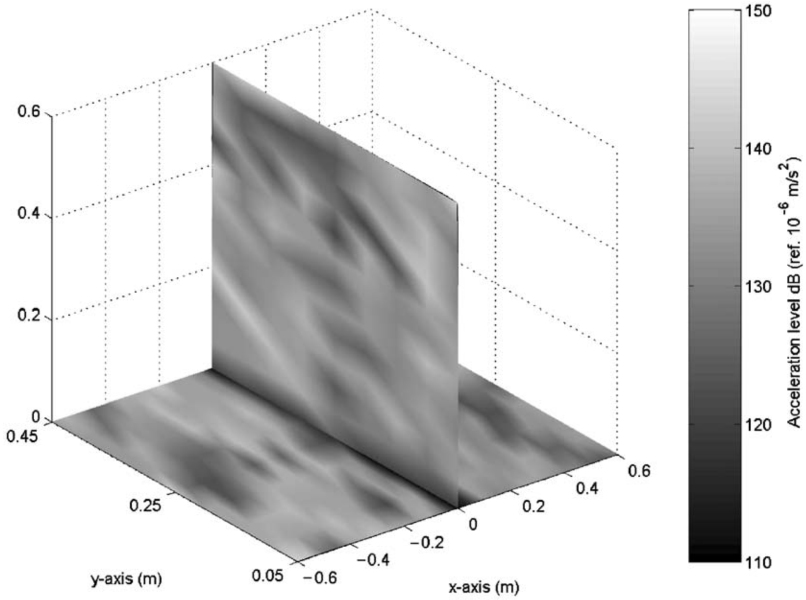

Fig. 20. Contour plot of the controlled response at 53.13 Hz for two dependently driven control forces at $(x_{s1}, y_{s1}) = (0.371, 0.25)$, $(x_{s2}, y_{s2}) = (0.371, 0.31)$ and two error sensors located at $(x_{e1}, y_{e1}) = (0.23, 0.25)$ and $(x_{e2}, y_{e2}) = (0.28, 0.25)$.

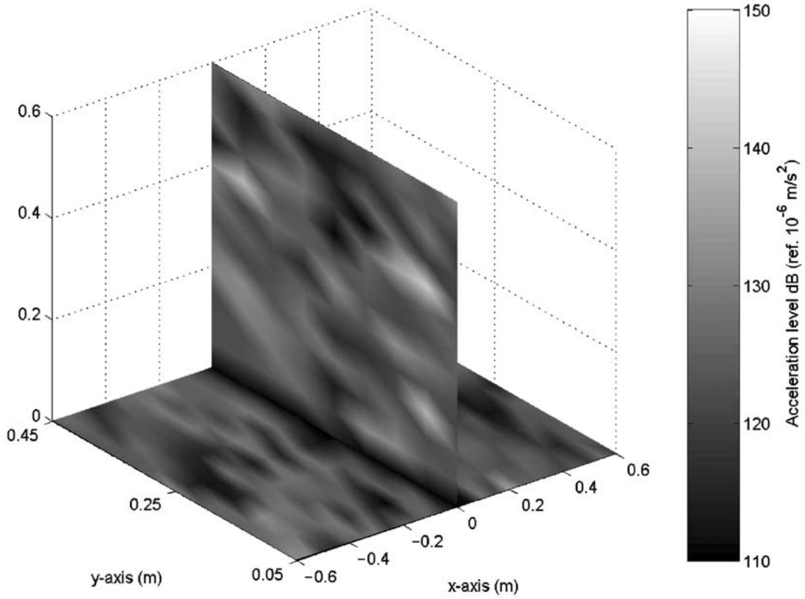

Fig. 21. Contour plot of the controlled response at 53.13 Hz for two independently driven control forces at $(x_{s1}, y_{s1}) = (0.371, 0.25)$, $(x_{s2}, y_{s2}) = (0.371, 0.31)$ and two error sensors located at $(x_{e1}, y_{e1}) = (0.23, 0.25)$ and $(x_{e2}, y_{e2}) = (0.28, 0.25)$.

achieved when the error sensors are located along the anti-nodal line, corresponding to the midway point along the width of the plate for this resonance frequency (Fig. 20). Fig. 21 shows the contour plot of the controlled response for the same control arrangement as Fig. 20, but with the control forces driven independently. Significantly better overall attenuation levels are achieved using independently driven control forces than the dependently driven control forces.

6. Conclusions

In this paper, active control of the dynamic response of a T-shaped plate subject to point force excitation has been carried out. Feedforward active control of the flexural vibrational levels in the coupled plate structure has been analytically and experimentally investigated using multiple control forces and error sensors, and for both dependently and independently driven control forces. It was shown that using two control forces to minimise the vibrational response at two error sensors, global attenuation of the primary frequency response was achieved, as well as global attenuation of the plate structure at a discrete resonance frequency. At arbitrary force and sensor locations, higher attenuation levels were achieved using independently driven control forces compared to dependently driven control forces.

Acknowledgements

Financial support for this work from the Australian Research Council and the Australian Defence Science and Technology Organisation, Maritime Platforms Division is gratefully acknowledged.

Appendix A

For the cross-shaped plate, $[E_p^i]$ is described as

$$\left[E_p^{1I}\right] = \left[\mathrm{e}^{-\mathrm{j}k_x x_1} \quad \mathrm{e}^{\mathrm{j}k_x x_1} \quad \mathrm{e}^{-k_n x_1} \quad \mathrm{e}^{k_n x_1} \quad 0 \quad 0 \quad 0 \quad 0 \quad 0 \quad 0 \quad 0 \quad 0 \quad 0 \quad 0 \quad 0 \quad 0\right]^{\mathrm{T}}, \quad x_p \leqslant x_1 \leqslant L_{x1}, \tag{A.1}$$

$$\left[E_p^{1II}\right] = \left[0 \quad 0 \quad 0 \quad 0 \quad \mathrm{e}^{-\mathrm{j}k_x x_1} \quad \mathrm{e}^{\mathrm{j}k_x x_1} \quad \mathrm{e}^{-k_n x_1} \quad \mathrm{e}^{k_n x_1} \quad 0 \quad 0 \quad 0 \quad 0 \quad 0 \quad 0 \quad 0 \quad 0\right]^{\mathrm{T}}, \quad 0 \leqslant x_1 \leqslant x_p, \tag{A.2}$$

$$\left[E_p^{2}\right] = \left[0 \quad 0 \quad 0 \quad 0 \quad 0 \quad 0 \quad 0 \quad 0 \quad \mathrm{e}^{-\mathrm{j}k_x x_2} \quad \mathrm{e}^{\mathrm{j}k_x x_2} \quad \mathrm{e}^{-k_n x_2} \quad \mathrm{e}^{k_n x_2} \quad 0 \quad 0 \quad 0 \quad 0\right]^{\mathrm{T}}, \quad 0 \leqslant x_2 \leqslant L_{x2}, \tag{A.3}$$

$$\left[E_p^{3}\right] = \left[0 \quad 0 \quad 0 \quad 0 \quad 0 \quad 0 \quad 0 \quad 0 \quad 0 \quad 0 \quad 0 \quad 0 \quad \mathrm{e}^{-\mathrm{j}k_x x_3} \quad \mathrm{e}^{\mathrm{j}k_x x_3} \quad \mathrm{e}^{-k_n x_3} \quad \mathrm{e}^{k_n x_3}\right]^{\mathrm{T}}, \quad 0 \leqslant x_3 \leqslant L_{x3}, \tag{A.4}$$

$[\alpha_p]$ is a 16×16 matrix for the T-shaped plate, and is obtained from the boundary conditions, and structural continuity and equilibrium equations. The boundary equations at the free edges $x_i = L_{xi}$ are for zero bending moment and net vertical shear [14]. At the driving force location of (x_p, y_p), four coupling equations are used to describe the continuity of the plate response under forced excitation [4,9]. The continuity relationships correspond to the continuity of the plate displacement, slope, moment and shear force. The boundary conditions at the structural junction of the coupled plates corresponding to $(x_i, z_i) = (0, 0)$ must also satisfy continuity and equilibrium of plate displacement, slope, moment and shear force [9].

$$[\alpha_p] =$$

$$\left[\begin{array}{cccc}
(-k_x^2 - vk_y^2)\mathrm{e}^{-\mathrm{j}k_xL_{x1}} & (-k_x^2 - vk_y^2)\mathrm{e}^{\mathrm{j}k_xL_{x1}} & (k_n^2 - vk_y^2)\mathrm{e}^{-k_nL_{x1}} & (k_n^2 - vk_y^2)\mathrm{e}^{k_nL_{x1}} \\
\mathrm{j}k_x(k_x^2 + (2-v)k_y^2)\mathrm{e}^{-\mathrm{j}k_xL_{x1}} & -\mathrm{j}k_x(k_x^2 + (2-v)k_y^2)\mathrm{e}^{\mathrm{j}k_xL_{x1}} & -k_n(k_n^2 - (2-v)k_y^2)\mathrm{e}^{-k_nL_{x1}} & k_n(k_n^2 - (2-v)k_y^2)\mathrm{e}^{k_nL_{x1}} \\
0 & 0 & 0 & 0 \\
0 & 0 & 0 & 0 \\
0 & 0 & 0 & 0 \\
0 & 0 & 0 & 0 \\
\mathrm{e}^{-\mathrm{j}k_xx_p} & \mathrm{e}^{\mathrm{j}k_xx_p} & \mathrm{e}^{-k_nx_p} & \mathrm{e}^{k_nx_p} \\
-\mathrm{j}k_x\mathrm{e}^{-\mathrm{j}k_xx_p} & \mathrm{j}k_x\mathrm{e}^{\mathrm{j}k_xx_p} & -k_n\mathrm{e}^{-k_nx_p} & k_n\mathrm{e}^{k_nx_p} \\
-k_x^2\mathrm{e}^{-\mathrm{j}k_xx_p} & -k_x^2\mathrm{e}^{\mathrm{j}k_xx_p} & k_n^2\mathrm{e}^{-k_nx_p} & k_n^2\mathrm{e}^{k_nx_p} \\
\mathrm{j}k_x^3\mathrm{e}^{-\mathrm{j}k_xx_p} & -\mathrm{j}k_x^3\mathrm{e}^{\mathrm{j}k_xx_p} & -k_n^3\mathrm{e}^{-k_nx_p} & k_n^3\mathrm{e}^{k_nx_p} \\
0 & 0 & 0 & 0 \\
0 & 0 & 0 & 0 \\
0 & 0 & 0 & 0 \\
0 & 0 & 0 & 0 \\
0 & 0 & 0 & 0 \\
0 & 0 & 0 & 0
\end{array}\right.$$

$$\begin{array}{cccc}
0 & 0 & 0 & 0 \\
0 & 0 & 0 & 0 \\
0 & 0 & 0 & 0 \\
0 & 0 & 0 & 0 \\
0 & 0 & 0 & 0 \\
0 & 0 & 0 & 0 \\
-\mathrm{e}^{-\mathrm{j}k_xx_p} & -\mathrm{e}^{\mathrm{j}k_xx_p} & -\mathrm{e}^{-k_nx_p} & -\mathrm{e}^{k_nx_p} \\
\mathrm{j}k_x\mathrm{e}^{-\mathrm{j}k_xx_p} & -\mathrm{j}k_x\mathrm{e}^{\mathrm{j}k_xx_p} & k_n\mathrm{e}^{-k_nx_p} & -k_n\mathrm{e}^{k_nx_p} \\
k_x^2\mathrm{e}^{-\mathrm{j}k_xx_p} & k_x^2\mathrm{e}^{\mathrm{j}k_xx_p} & -k_n^2\mathrm{e}^{-k_nx_p} & -k_n^2\mathrm{e}^{k_nx_p} \\
-\mathrm{j}k_x^3\mathrm{e}^{-\mathrm{j}k_xx_p} & \mathrm{j}k_x^3\mathrm{e}^{\mathrm{j}k_xx_p} & k_n^3\mathrm{e}^{-k_nx_p} & -k_n^3\mathrm{e}^{k_nx_p} \\
1 & 1 & 1 & 1 \\
-\mathrm{j}k_x & \mathrm{j}k_x & -k_n & k_n \\
0 & 0 & 0 & 0 \\
\mathrm{j}\left(k_x^3 + k_p^4/k_L\right) & -\mathrm{j}\left(k_x^3 - k_p^4/k_L\right) & -\left(k_n^3 - \mathrm{j}k_p^4/k_L\right) & \left(k_n^3 + \mathrm{j}k_p^4/k_L\right) \\
\mathrm{j}\left(k_x^3 + k_p^4/k_L\right) & -\mathrm{j}\left(k_x^3 - k_p^4/k_L\right) & -\left(k_n^3 - \mathrm{j}k_p^4/k_L\right) & \left(k_n^3 + \mathrm{j}k_p^4/k_L\right) \\
-k_x^2 - vk_y^2 & -k_x^2 - vk_y^2 & k_n^2 - vk_y^2 & k_n^2 - vk_y^2
\end{array}$$

$$
\begin{array}{cccc}
0 & 0 & 0 & 0 \\
0 & 0 & 0 & 0 \\
\left(-k_x^2 - vk_y^2\right)\mathrm{e}^{-\mathrm{j}k_xL_{x2}} & \left(-k_x^2 - vk_y^2\right)\mathrm{e}^{\mathrm{j}k_xL_{x2}} & \left(k_n^2 - vk_y^2\right)\mathrm{e}^{-k_nL_{x2}} & \left(k_n^2 - vk_y^2\right)\mathrm{e}^{k_nL_{x2}} \\
\mathrm{j}k_x\left(k_x^2 + (2-v)k_y^2\right)\mathrm{e}^{-\mathrm{j}k_xL_{x2}} & -\mathrm{j}k_x\left(k_x^2 + (2-v)k_y^2\right)\mathrm{e}^{\mathrm{j}k_xL_{x2}} & -k_n\left(k_n^2 - (2-v)k_y^2\right)\mathrm{e}^{-k_nL_{x2}} & k_n\left(k_n^2 - (2-v)k_y^2\right)\mathrm{e}^{k_nL_{x2}} \\
0 & 0 & 0 & 0 \\
0 & 0 & 0 & 0 \\
0 & 0 & 0 & 0 \\
0 & 0 & 0 & 0 \\
0 & 0 & 0 & 0 \\
0 & 0 & 0 & 0 \\
0 & 0 & 0 & 0 \\
\mathrm{j}k_x & -\mathrm{j}k_x & k_n & -k_n \\
-\mathrm{j}k_x & \mathrm{j}k_x & -k_n & k_n \\
0 & 0 & 0 & 0 \\
\mathrm{j}\left(k_x^3 - k_p^4/k_L\right) & -\mathrm{j}\left(k_x^3 + k_p^4/k_L\right) & -\left(k_n^3 + \mathrm{j}k_p^4/k_L\right) & -\left(k_n^3 - \mathrm{j}k_p^4/k_L\right) \\
-k_x^2 - vk_y^2 & -k_x^2 - vk_y^2 & k_n^2 - vk_y^2 & k_n^2 - vk_y^2
\end{array}
$$

$$
\left.
\begin{array}{cccc}
0 & 0 & 0 & 0 \\
0 & 0 & 0 & 0 \\
0 & 0 & 0 & 0 \\
0 & 0 & 0 & 0 \\
\left(-k_x^2 - vk_y^2\right)\mathrm{e}^{-\mathrm{j}k_xL_{x3}} & \left(-k_x^2 - vk_y^2\right)\mathrm{e}^{\mathrm{j}k_xL_{x3}} & \left(k_n^2 - vk_y^2\right)\mathrm{e}^{-k_nL_{x3}} & \left(k_n^2 - vk_y^2\right)\mathrm{e}^{k_nL_{x3}} \\
-\mathrm{j}k_x\left(k_x^2 + (2-v)k_y^2\right)\mathrm{e}^{\mathrm{j}k_xL_{x3}} & -\mathrm{j}k_x\left(k_x^2 + (2-v)k_y^2\right)\mathrm{e}^{\mathrm{j}k_xL_{x2}} & -k_n\left(k_n^2 - (2-v)k_y^2\right)\mathrm{e}^{-k_nL_{x3}} & k_n\left(k_n^2 - (2-v)k_y^2\right)\mathrm{e}^{k_nL_{x3}} \\
0 & 0 & 0 & 0 \\
0 & 0 & 0 & 0 \\
0 & 0 & 0 & 0 \\
0 & 0 & 0 & 0 \\
1 & 1 & 1 & 1 \\
0 & 0 & 0 & 0 \\
\mathrm{j}k_x & -\mathrm{j}k_x & k_n & -k_n \\
\mathrm{j}\left(k_x^3 - k_p^4/k_L\right) & -\mathrm{j}\left(k_x^3 + k_p^4/k_L\right) & -\left(k_n^3 + \mathrm{j}k_p^4/k_L\right) & \left(k_n^3 - \mathrm{j}k_p^4/k_L\right) \\
0 & 0 & 0 & 0 \\
-k_x^2 - vk_y^2 & -k_x^2 - vk_y^2 & k_n^2 - vk_y^2 & k_n^2 - vk_y^2
\end{array}
\right]
$$

References

[1] A.J. Young, C.H. Hansen, Control of flexural vibration in stiffened structures using multiple piezoceramic actuators, *Applied Acoustics* 49 (1996) 17–48.

[2] S.J. Elliott, L. Billet, Adaptive control of flexural waves propagating in a beam, *Journal of Sound and Vibration* 163 (1993) 295–310.

[3] B.J. Brevar, C.R. Fuller, Active control of coupled waved propagation in fluid-filled elastic shells, *Journal of the Acoustical Society of America* 94 (1993) 1467–1475.

[4] X. Pan, C.H. Hansen, Active control of vibratory power transmission along a semi-infinite plate, *Journal of Sound and Vibration* 184 (1995) 585–610.

[5] J.C. Lee, J.C. Chen, Active control of sound radiation from a rectangular plate excited by a line moment, *Journal of Sound and Vibration* 220 (1999) 99–115.

[6] R.L. Clark, C.R. Fuller, Optimal placement of piezoelectric actuators and polyvinylidene fluoride error sensors in active structural acoustic control approaches, *Journal of the Acoustical Society of America* 92 (1992) 1521–1533.

[7] P. Sergent, D. Duhamel, Optimal placement of sources and sensors with the minimax criterion for active control of a one-dimensional sound field, *Journal of Sound and Vibration* 207 (1997) 537–566.

[8] K. Hiramoto, H. Doki, G. Obinata, Optimal sensor/actuator placement for active vibration control using explicit solution of algebraic riccati equation, *Journal of Sound and Vibration* 229 (2000) 1057–1075.

[9] J. Keir, N.J. Kessissoglou, C.J. Norwood, An analytical investigation of single actuator and error sensor control in connected plates, *Journal of Sound and Vibration* 271 (2004) 635–649.

[10] C.R. Fuller, S.J. Elliott, P.A. Nelson, *Active Control of Vibration*, Academic Press, London, 1996.

[11] N. Farag, Comparison of Vibration Properties of Flat Panels of Various Forms of Construction, Master of Science Thesis, Cranfield Institute of Technology, 1979.

[12] S.D. Snyder, G. Vokalek, EZ-ANC User's Guide, Causal Systems Pty Ltd, 1994.

[13] M.P. Norton, *Fundamentals of Noise and Vibration Analysis for Engineers*, Cambridge University Press, Cambridge, 1989.

[14] S. Timoshenko, S. Woinowsky-Krieger, *Theory of Plates and Shells*, 2nd ed., McGraw-Hill, New York, 1959.